Advances in Applied Mathematics and Mechanics
Adv. Appl. Math. Mech., Vol. **17**, No. 1, pp. 1-30

DOI: 10.4208/aamm.OA-2024-0122
February 2025

Method to Improve Heat Extraction in Enhanced Geothermal Systems with Heterogeneous Fracture Network

Qiang Huang[1], Ning Guo[1], Haibo Huang[1], Jie Yu[2], Gang Pei[1] and Maobin Hu[1,*]

[1] *School of Engineering Science, University of Science and Technology of China, Hefei, Anhui 230026, China*
[2] *Hefei Institutes of Physical Science, Chinese Academy of Sciences, Hefei, Anhui 230031, China*

Received 5 June 2024; Accepted (in revised version) 3 July 2024

Abstract. In typical EGS fracturing projects, the fracture network is denser in the region close to the fracturing wells. The distribution of fractures has a significant impact on the heat extraction performance of enhanced geothermal system (EGS). In order to avoid premature thermal breakthrough and improve the thermal extraction efficiency, this paper studies the heat extraction performance of EGS in heterogeneous fractured reservoirs under different injection-production methods. First, a heterogeneous discrete fracture network generation method based on relative pressure distribution is developed. A thermo-hydraulic-mechanical (THM) coupling model is established to simulate the fluid flow and heat transfer in reservoirs. The heat extraction performance under different production and injection modes is compared with different fracture densities. The results show that injection in the dense side of the anti-parallel well configuration will be more efficient for heat extraction. Under the condition of same injection mass flow rate, the heat extraction performance is positively correlated with the fracture density. Although sparse-side injection is not conducive to fluid flow, under the condition of same injection mass flow rate with anti-parallel well configuration, it will improve the thermal extraction performance.

AMS subject classifications: 76S05, 35Q99

Key words: Enhanced geothermal systems, heterogeneous discrete fracture network, injection and production modes, heat extraction.

*Corresponding author.
Email: humaobin@ustc.edu.cn (M. Hu)

1 Introduction

As one of the most potential sustainable energy sources [1,2], geothermal energy has large reserves and is widely distributed in the world [3–5]. More than 90% of the available geothermal resources are stored in the hot dry rock (HDR) [6,7]. To facilitate heat extraction from HDR, the enhanced geothermal system (EGS) fractures HDR to obtain interconnected fracture networks. The fracturing methods include hydraulic fracturing [8,9], gas fracturing [10–12], thermal stress fracturing [13–15] and chemical stimulation [16]. During the fracturing process, the newly generated fractures will interact with the original fractures to produce complex fracture structures [17–19]. Because the HDR is located deep in the formation and the environment is complex, the experimental study of fractured reservoir is difficult [20]. Therefore, numerical simulation of geothermal reservoir plays an important role in the design and planning of geothermal projects. There are still some difficulties in the description of actual fractured reservoirs [21]. Especially, most literatures adopt homogeneous fracture network to represent the fractured reservoirs.

In fact, in the fracturing process, the distribution of fractures in the reservoir is highly heterogeneous. The density of the fracture network is higher in the region near the fracturing well. The performance of thermal recovery in EGS depends significantly on the distribution of the fracture network in the reservoir. Additionally, an efficient well layout can improve HDR resource extraction. Optimizing thermal recovery in fractured reservoirs with heterogeneous fracture networks is crucial for the development of geothermal resources. Therefore, this paper studies the thermal extraction performance of heterogeneous fractured reservoirs under different injection and production methods (different well layout).

In order to improve the heat extraction efficiency of EGS, researchers have carried out many interesting studies on well layout and fracture structure. The geometric structure of fracture network has a great impact on the performance of fractured reservoir. The appropriate well layout is also helpful to improve the heat recovery efficiency of hot dry rock. Ma et al. studied the effects of different well layout schemes with a specific injection-production ratio on the EGS thermal recovery performance [22]. They found that longer production and injection well spacing was conducive to the thermal recovery of reservoirs, and the production temperature had a greater competitiveness when one injection and one production pattern was used. Li et al. conducted probabilistic research on the heat extraction performance of EGS under discrete fracture network [23], and the results showed that probabilistic performance evaluation was helpful to design and optimize the efficient heat recovery of deep geothermal reservoir. Zhang et al. studied fluid driven fracture propagation in naturally fractured rock mass [24]. The results show that due to the highly inhomogeneous of natural fractured rock mass, hydraulic fracturing stimulation in this medium may lead to complex fracturing system rather than simple planar fractures. Xu et al. studied the joint effects of fracture geometry and thermal stress on the THM behavior of EGS [25]. The results show that the geometric connectivity of fracture network plays a leading role in determining the THM process and thermal

performance of EGS. When the connectivity of fracture system ranges from 15 to 35, satisfactory thermal performance is often obtained. Yu et al. studied the heat extraction efficiency of eight different complex fracture geometries, and compared the contribution of primary and secondary fractures to EGS heat extraction in multilateral-wells [26]. They found that the establishment of a fracture network with long fractures and less fractures near the well is more conducive to the improvement of EGS efficiency of multilateral wells. Liao et al. studied the heat extraction of EGS in a fracture–wells system [27], in which injection wells and production wells are connected through horizontal fractures. The results showed that the outlet temperature decreased rapidly from 260°C to 100°C within 2 months after the thermal breakthrough. Although the above research discussed the influence of different well layout and fracture parameters from different perspectives, it did not consider the nonuniformity of fracture spatial distribution. In practice, the spatial distribution of fracture network is non-uniform, the fracture network is denser and the size of fracture is larger in the region close to the fracturing wells [28]. Previous studies have shown that the fracture network is the main heat transfer channel for fluid, and its geometric structure has a great impact on the performance of heat extraction in fractured reservoirs [29]. In addition, the heat extraction process of HDR reservoir involves fluid flow, heat transfer, rock mass deformation, and the coupling between physical fields is complex. Hence, it is important to comprehensively understand the influence of different production and injection methods on the thermal performance of heterogeneous fractured reservoirs under thermo-hydraulic-mechanical (THM) coupling.

In this paper, a heterogeneous discrete fracture network generation method based on pressure distribution is developed, and a two-dimensional thermo-hydraulic-mechanical coupling model is established to study the influence of different injection-production methods on thermal extraction of heterogeneous fractured reservoirs. Furthermore, the evolution of the stress field during the heat extraction process was analyzed and sensitivity analysis on key parameters was conducted. Extensive simulations show that, the dense-side injection for the anti-parallel well configuration is more efficient for heat extraction. Under the condition of same injection mass flow rate, the heat extraction performance is positively correlated with the fracture density. For the anti-parallel well configuration with the same mass flow rate, the thermal extraction performance of the reservoir can be effectively improved by using sparse-side injection or increasing fracture density. It is evident that an excessive mass flow rate and injection pressure are not conducive to thermal extraction of the reservoir. These results can sharpen the understanding of the flow and heat transfer in the heterogeneous fracture network and provide reference for Geothermal Engineering.

The rest of this paper is organized as follows. Section 2 introduces the fracture generation method and the thermo-hydraulic-mechanical coupled model. Section 3 presents the parameter setting of simulation. The results are presented and discussed in Section 4. Finally, Section 5 summarizes the work.

2 Thermo-hydraulic-mechanical coupled model for heterogeneous fractures

In this section, the enhanced geothermal system (EGS) is described and a numerical thermo-hydraulic-mechanical coupled model for simulating fluid flow and heat transfer processes in fractured reservoirs is presented.

Fig. 1 shows the schematic diagram of two different doublet designs of EGS system [30]. The parallel doublet system (Fig. 1(a)) means that the injection well and the production well are drilled in the same plane and direction. In the anti-parallel doublet system (Fig. 1(b)), the direction of injection well and production well is opposite. In both systems, the spacing between the wells remains constant.

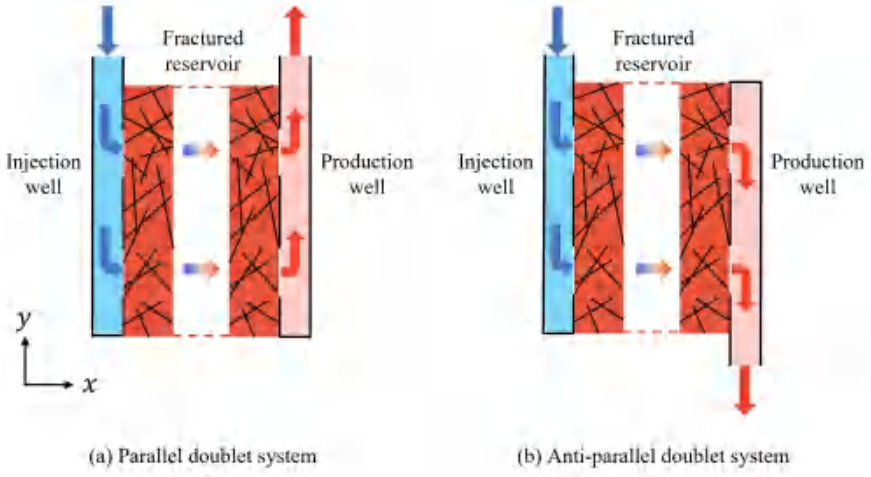

Figure 1: Schematic of different doublet EGS systems: (a). Parallel well doublet system. (b). Anti-parallel well doublet system.

2.1 Heterogeneous fracture networks model

Because the real fractured reservoir is located in the deep formation and the geometric structure of fractures is complex, it is difficult to obtain the geometric information of the fracture network in the whole reservoir. Most literatures assumed that the fracture network is uniform. Little attention has been paid on the effect of heterogeneous fracture networks. In real fracturing process, the distribution of fracture network is non-uniform due to the pressure distribution in the fracturing process. In this paper, the concept of relative pressure distribution in reservoir is first introduced in the generation process of discrete fracture networks. By coupling the relative pressure distribution of reservoir to the generation process of discrete fracture network, the heterogeneity of fracture distribution in fractured reservoir can be better characterized.

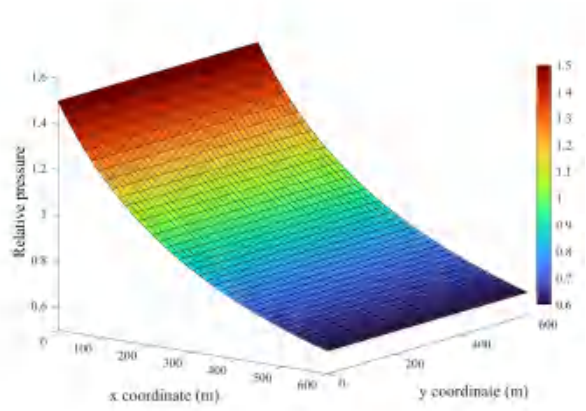

Figure 2: Relative pressure distribution in the reservoir during fracturing.

Without loss of generality, it is assumed that, in the fracturing process, the pressure is higher and the fracture size is larger in the region close to the fracturing wells. Typical distribution of relative pressure in the reservoir is shown in Fig. 2. Assuming that a fracturing well is located at the left side of the reservoir, the pressure distribution can be simplified so that its value remains constant in the y-direction and is inversely proportional to x-coordinate:

$$P_r = \frac{L}{(x+2L/3)}, \tag{2.1}$$

where x is the distance from the fracturing well, and L is the scale of the model domain. In order to facilitate subsequent calculation, the value of relative pressure is controlled around 1.

The specific flowchart for generating heterogeneous discrete fracture networks is shown in Fig. 3. As in previous studies [31–33], it is reasonable to use probabilities to characterize the fracture network from the perspective of statistics. In this paper, we assume that the direction of the fractures obeys uniform distribution. Since fracture density is expressed as the total length of fractures per unit area, increasing fracture density can be achieved either by increasing the number of fractures or by increasing the length of fractures in the area. Here, the location of the fracture has a higher probability of occurring in the region near the fracturing wells, while the trace length of the fractures obeys power-law distribution. The density function of the power-law statistical model is shown as follow [34]:

$$n(l) = bl^{-a}, \quad l \in [l_{\min}, l_{\max}], \tag{2.2}$$

where l is the fracture length; a is the power-law length exponent, which is ranged between 1 and 3 ; and b is the density term. The intrinsic characteristic lengths in this model are the minimum and maximum fracture lengths, $l_{\min}$ and $l_{\max}$. In numerical simulations,

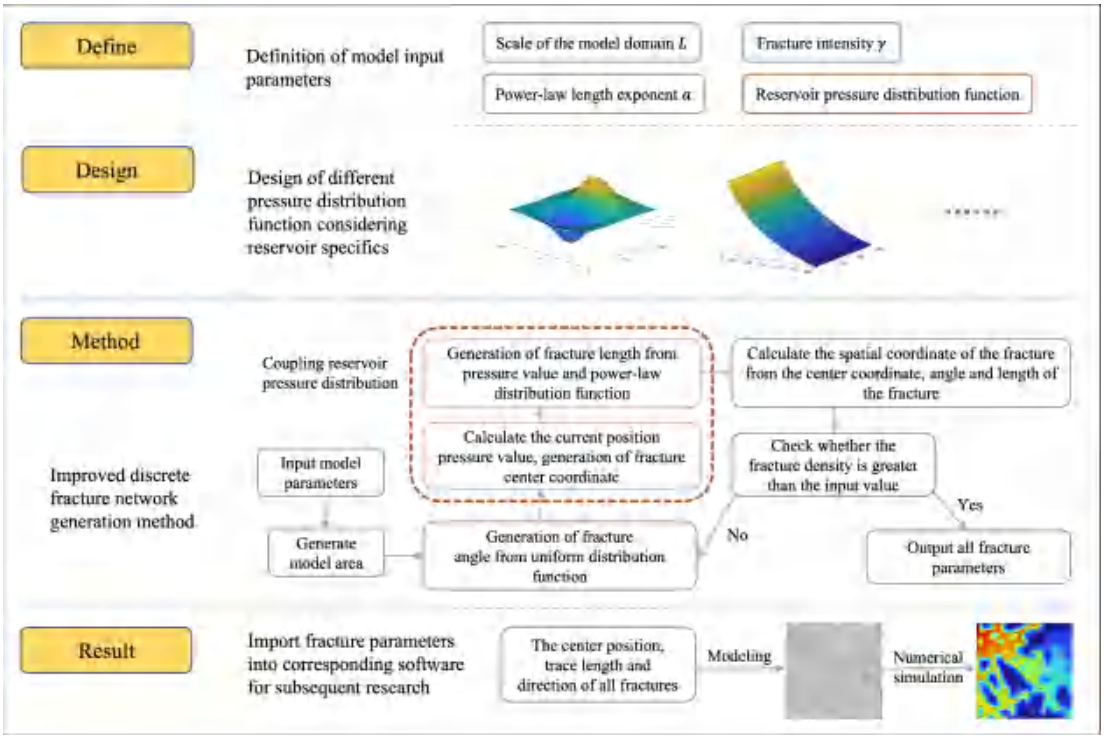

Figure 3: Flowchart for generating heterogeneous discrete fracture networks.

it is usually satisfied as $l_{\min} \ll L \ll l_{\max}$, where L is the scale of the model domain. Finally, to reflect the effect of relative pressure, after obtaining the fracture trace length using the power-law distribution above, the final trace length of the fracture is obtained by multiplying it with the relative pressure at the corresponding position. With this treatment, we can generate fractures with longer trace lengths with a high probability at locations of high relative pressure.

The fracture intensity γ (denotes fracture density) is the total length of fractures per unit area [25,34]

$$\gamma = \frac{1}{L^2} \int n(l,L) l' dl, \tag{2.3}$$

where l' denotes the length of fractures in region, L^2 is size of the region.

2.2 Thermal-hydraulic-mechanical model

2.2.1 Basic assumptions

From the above description, we can make the following assumptions for the thermo-hydraulic-mechanical model.

(1). The reservoir consists of a fracture network and a rock matrix. The rock matrix can be described as a continuous porous medium whose physical properties are homogeneous and isotropic, and the deformation conforms to linear elastic model. The permeability of rock matrix is much lower than that of fracture, and fracture is the main channel of fluid flow.

(2). The working fluid is water, and the pressure in the reservoir is high enough that no phase transition occurs in the simulation process.

(3). The fluid flow follows Darcy's law [7,20,28,35], and the heat exchange between the reservoir and the fracture network is realized by heat conduction and heat convection [36–38], which can be described by local heat balance.

(4). All fractured reservoirs and wells are in the xy plane, where the gravity effect can be ignored.

(5). No new fractures will be generated during the heat extraction process.

Based on the above assumptions, the control equations for the thermo-hydraulic-mechanical coupling model can be derived in the fractured reservoir.

2.2.2 Conservation of mass equation

By calculating the mass conservation equations for the rock matrix and fractures, the seepage velocity field of the fluid flow in the model can be obtained.

Controlling equations in the rock matrix can be described by mass conservation equation and Darcy's law as follow [22,26]

$$S_m \frac{\partial p}{\partial t} + \nabla u_m + Q_m = 0, \tag{2.4}$$

where p denotes the hydraulic pressure, Pa; t is the time of simulation, s; S_m denotes the specific storage of the rock matrix, $1/\mathrm{Pa}$; ∇ represents the spatial gradient operator; u_m denotes the flow velocity in the rock matrix, $\mathrm{m/s}$; Q_m is the fluid source and sink term in the rock matrix, $1/s$. According to the assumptions, the flow velocity of the fluid can be described by Darcy's law:

$$u_m = -\frac{\kappa_m}{\eta}\left(\nabla p + \rho_f g \nabla z\right), \tag{2.5}$$

where κ_m denotes the permeability of the rock matrix, m^2; η denotes the dynamic viscosity of the fluid, Pa·s; ρ_f indicates the density of the fluid, $\mathrm{kg/m^3}$; g is the gravitational acceleration, m/s^2.

The controlling equation for the flow in the fracture can be described as follows [22, 26]:

$$d_f S_f \frac{\partial p}{\partial t} + \nabla_\tau \left(d_f u_f\right) + Q_f = 0, \tag{2.6a}$$

$$u_f = -\frac{\kappa_f}{\eta}\left(\nabla_\tau p + \rho_f g \nabla_\tau z\right), \tag{2.6b}$$

where d_f denotes the aperture of the fracture, m; S_f denotes the specific storage of the facture, $1/\mathrm{Pa}$; ∇_τ denotes the gradient operator restricted to the fracture's tangential plane; u_f denotes flow velocity in the fracture, $\mathrm{m/s}$; and can be described by Darcy's law; Q_f denotes the source and sink term on the fracture plane, $\mathrm{m/s}$. And κ_f denotes the permeability of the fractures.

The dynamic viscosity of water is affected by temperature, $\eta = v\rho_f$ in which v is the kinematic viscosity of water. The commonly used empirical formula for kinematic viscosity is [39, 40]

$$v = \frac{1.775}{1 + 0.0337T_f + 0.000221T_f^2}. \tag{2.7}$$

Where T_f is the fluid temperature. In this work, the dynamic viscosity of water is described by the following empirical formula [41]:

$$\eta\left(T_f\right) = \begin{cases} 1.38 - 0.0212T_f + 1.3605\times10^{-4}T_f^2 - 4.6454\times10^{-7}T_f^3 + 8.9043\times10^{-10}T_f^4 \\ \quad -9.0791\times10^{-13}T_f^5 + 3.8457\times10^{-16}T_f^6, \quad 273.15K \le T_f \le 413.15K, \\ 0.004 - 2.1075\times10^{-5}T_f + 3.8578\times10^{-8}T_f^2 - 2.3973\times10^{-11}T_f^3, \\ \qquad\qquad 413.15K \le T_f \le 553.15K, \end{cases} \tag{2.8}$$

the dynamic viscosity of water is directly related to temperature, coupling the fluid flow and heat transfer process in the reservoir.

2.2.3 Conservation of energy equation

The temperature field of the solution domain can be obtained by solving the energy conservation equation in the rock medium and fractures.

In geothermal reservoirs, the transfer of heat is achieved by heat conduction and heat convection, heat convection occurs mostly in fractures, while heat conduction is the main heat transfer process between rock matrix and fractures. In this study, the theory of local thermal equilibrium is introduced to simplify the calculation. It is assumed that the thermophysical properties of the rock matrix, fractures and fluids in a computational cell can be expressed by effective values. The effective heat capacity and effective thermal conductivity are weighted averages of the water and rock matrix values [23, 42]

$$\left(\rho C_p\right)_{\text{eff}} = \varphi\left(\rho_f C_f\right) + (1-\varphi)\left(\rho_m C_m\right), \tag{2.9a}$$

$$\lambda_{\text{eff}} = \varphi\lambda_f + (1-\varphi)\lambda_m, \tag{2.9b}$$

where $(\rho C_p)_{\text{eff}}$ denotes the effective heat capacity; λ_{eff} denotes the effective thermal conductivity, $W/(m\cdot K)$; φ denotes porosity; C_f and C_m denote the heat capacity of water and rock matrix respectively, $J/(\text{kg}\cdot\text{K})$; ρ_f and ρ_m denote the density of water and rock matrix respectively, kg/m^3; λ_f and λ_m denote the thermal conductivity of water and rock matrix respectively, $W/(m\cdot K)$.

According to the energy conservation theorem, the controlling equation for the temperature field in the rock matrix and fracture can be described as following [23, 42]:

$$(\rho C_p)_{\text{eff}} \frac{\partial T}{\partial t} + C_f u_m \nabla T - \nabla\cdot(\lambda_{\text{eff}} \nabla T) + q_{h,m} = 0, \tag{2.10a}$$

$$d_f (\rho C_p)_{\text{eff}} \frac{\partial T}{\partial t} + d_f C_f u_f \nabla T - \nabla\cdot\left(d_f \lambda_{\text{eff}} \nabla T\right) + q_{h,f} = 0, \tag{2.10b}$$

where $q_{h,m}$ is heat source and sink in the rock matrix, W/m^3; $q_{h,f}$ is heat source and sink in the fracture, W/m^2; T is the temperature, K; u is the flow velocity, m/s. The subscripts m and f represent rock matrix and fracture, respectively.

2.2.4 Stress balance equation

According to Hooke's law, the governing equation of linear elastic model can be described as following [43]:

$$\frac{3(1-v)}{1+v}\nabla^2\sigma_{\text{total}} + \nabla\cdot\mathbf{G} - \frac{2(1-2v)}{1+v}\left(\alpha_B \nabla p + 3\alpha_T K \nabla^2 T\right) = 0, \tag{2.11}$$

where v is Poisson's ratio, σ_{total} is the mean total stress, $\mathbf{G}$ denotes the body force, α_B is the Biot's constants, α_T is the thermal expansion coefficient and K is the bulk module for rock matrix.

The mechanical processes in EGS will cause the permeability of pores and fractures in rock matrix to change with stress and strain. In a dense fracture network, fractures act as the main channel of fluid flow, changes in stress and strain can bring considerable changes to the permeability of the fractures and thus alter the fluid flow behavior in the reservoir.

In this work the porosity of the fracture is considered as a constant and the permeability can be expressed as following [44]:

$$\kappa_f = \kappa_{f0}\exp\left[-\left(\frac{\sigma_n'}{\gamma}\right)\right], \quad \sigma_n' = \sigma_n - \alpha_B p, \tag{2.12}$$

where κ_{f0} is initial permeability, σ_n' and σ_n are effective normal stress and total normal stress of fractures, respectively. γ is set as 10MPa.

2.3 Model verification

Due to the complex and coupled physical processes of fluid flow, heat transfer, and reservoir deformation involved in numerical simulation in reservoirs, the accuracy of numerical models for Multiphysics field coupled numerical simulation is crucial. In this section,

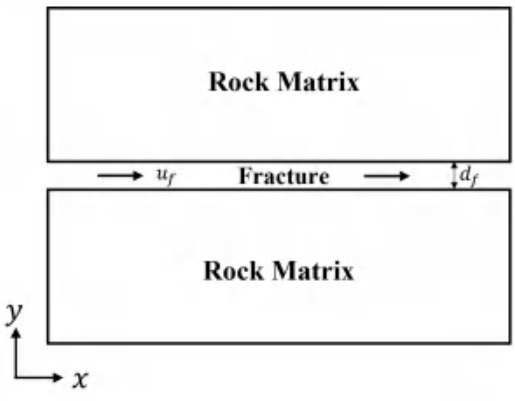

Figure 4: Schematic diagram of single fracture model.

model validation was conducted on the coupling process of thermo-hydraulic (TH) and thermal-hydraulic-mechanical (THM), respectively. In this work, the commercial software COMSOL is used to solve the coupling model.

In order to verify the reliability and accuracy of the TH coupling model, the simulation results of single fracture model were compared with analytical solution. The analytical solution proposed by Lauwerier et al. [45] and Barends et al. [46] describes the temperature variation within a single fracture. The schematic diagram of single fracture model is shown in Fig. 4. The model consists of a fracture and a rock matrix. In the derivation of analytical solution, it is assumed that the model extends infinitely along the x and y directions. The initial temperature of the reservoir is constant. A fluid with a constant temperature is injected at a constant rate from the left side of the fracture. Fracture aperture keeps constant, and the rock matrix is considered to be homogeneous and isotropic. Under the above assumptions, the analytic solution can be described as following:

$$T = T_0 + (T_{in} - T_0)\,\mathrm{erfc}\left(\frac{\lambda_m x}{\rho_f c_f d_f}\sqrt{\frac{\rho_m c_m}{u_f \lambda_m (u_f t - x)}}\right) U\left(t - \frac{x}{u_f}\right), \tag{2.13}$$

where T_0 denote the initial temperature; T_{in} denotes the injection temperature; d_f is the fracture aperture; erfc is the complementary error function and U is the unit step function; λ denotes the thermal conductivity; ρ is the density; c is the heat capacity; u is the flow velocity. The subscripts m and f represent rock matrix and fracture, respectively.

In numerical simulation, a rock matrix area with size 100m$\times$100m is generated and the horizontal fracture is located in the middle of the matrix. The parameter values for the analytical solution and the numerical simulation are listed in Table 1 [35,36,38,47,48]. The total simulation period is 3000 days, and each time step is 1 day. Fig. 5 shows the comparison of analytical and numerical solutions. Fig. 5(a) describes the variation of temperature at different locations (x=20m, x=40m and x=60m) in the fracture. Fig. 5(b)

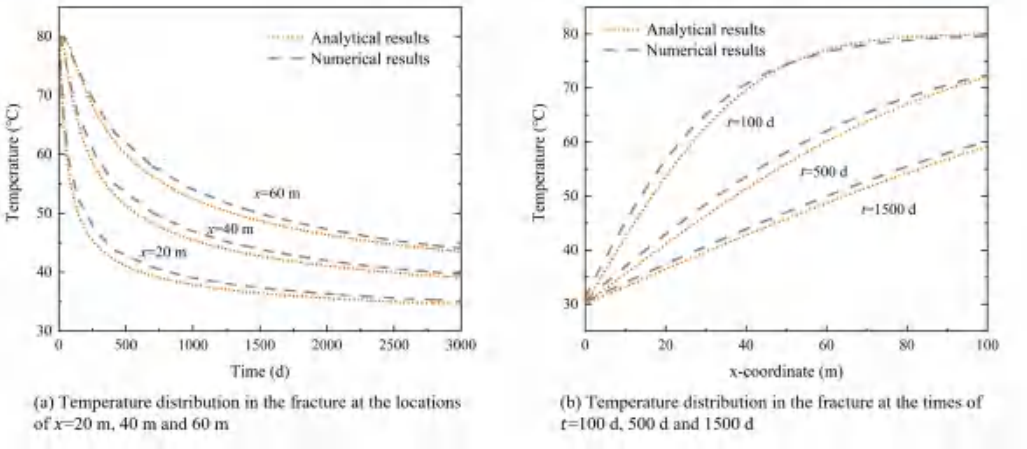

(a) Temperature distribution in the fracture at the locations of x=20 m, 40 m and 60 m

(b) Temperature distribution in the fracture at the times of t=100 d, 500 d and 1500 d

Figure 5: Comparison of analytical and numerical solutions for temperature in the fracture.

shows the temperature distribution in the fracture at different time steps (t=100d, t=500d and t=1500d). The good agreement between the numerical and analytical solutions, with errors within acceptable limits, indicates the accuracy of numerical model. The small discrepancy between numerical and analytical solutions may be due to the fact that in the analytical solution the geometric region is assumed to be infinitely extended in the x and y directions, whereas in the numerical model the geometric region is finite. Moreover, errors in the meshing of the numerical model and discretization during the numerical simulation may also lead to errors in the calculation of numerical results.

The THM coupling model is validated by simulating the linear elastic column model as shown in Fig. 6. The analytical solution proposed by Bai et al. [49] describes the variation of temperature, pore pressure and displacement. In the numerical model, the initial temperature and the pore pressure are set to 283.15K and 0.1MPa, respectively. The

Table 1: Parameters for TH model validation [35, 36, 38, 47, 48].

Parameters	Unit	Value
Rock density ρ_m	kg/m^3	2700
Rock heat capacity c_m	$J/(\text{kg}\cdot K)$	1000
Rock heat conductivity λ_m	$W/(m\cdot K)$	2.8
Water density ρ_f	kg/m^3	1000
Water heat capacity c_f	$J/(\text{kg}\cdot K)$	4200
Water viscosity η	Pa·s	0.001
Fracture aperture d_f	m	0.001
Flow velocity u_f	m/s	0.01
Initial temperature T_0	°C	80
Injection temperature T_{in}	°C	30

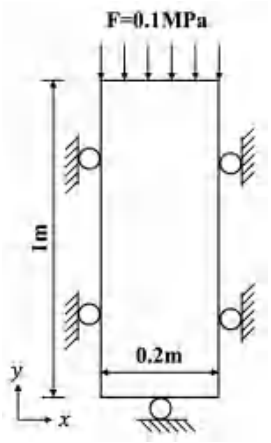

Figure 6: Schematic diagram of linear elastic column model.

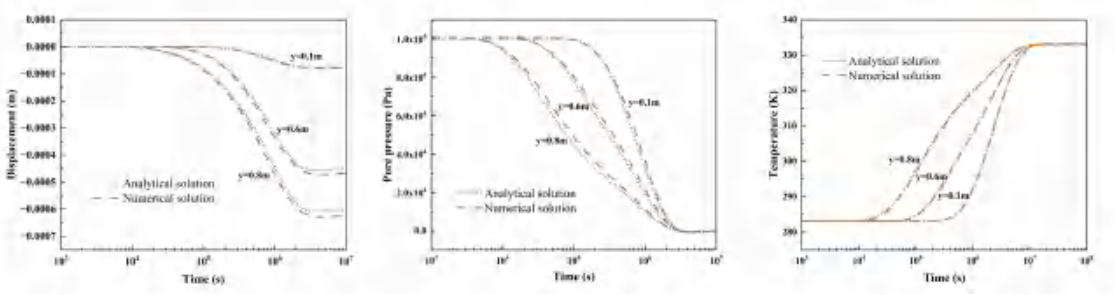

Figure 7: The verification of THM coupling model.

upper boundary is subjected to an external pressure of 0.1MPa, and the temperature and hydraulic conditions of the upper boundary are 333.15K and 0MPa, respectively. Other boundary conditions are adiabatic, no flow and zero displacement boundary conditions. The material parameters used in the numerical model are listed in Table 2. Fig. 7 shows the variation of displacement, pore pressure and temperature at different positions ($y = 0.1$m, $y = 0.6$m, $y = 0.8$m). The results of the numerical solution are in good agreement with those of the analytical solution, and the difference between the two is in an acceptable range, indicating the accuracy and reliability of the numerical model.

3 Model setup

3.1 Discrete fracture networks

A discrete fracture network is established in a square domain of $L = 600$m. The left side of the domain is set to fracture wells, and the relative pressure distribution is shown

Table 2: Parameters for THM model validation [50].

Parameters	Value
Bulk modulus of solid	2×10^{10}Pa
Bulk modulus of water	5×10^{9}Pa
Elastic modulus	60 MPa
Biot coefficient	1
Poisson ratio	0.4
Thermal expansion coefficient	3×10^{-7}1/K
Porosity	0.4
Solid heat conductivity	0.5W/K/m
Solid heat capacity	800J/kg/K

in Fig. 2. The fracture length follows a power-law distribution with minimum length $l_{\min}=L/50=12$m and maximum length $l_{\max}=50\times L=3\times10^{4}$m. The spatial and directional distributions of fractures are assumed to be random. We studied a typical heterogeneous discrete fracture network at fracture power-law length exponent $a=2.1$, fracture intensity $\gamma=0.05\text{m}^{-1}$ and three heterogeneous fracture networks with fracture intensity $\gamma=0.25,0.05,0.075\text{m}^{-1}$

3.2 Numerical model design and boundary conditions

Due to the high permeability of the fracture network, the structure of the fracture network has a significant effect on the heat extraction performance of fractured reservoirs. In this study, the relative pressure distribution in the reservoir during the fracturing process is coupled with the generation of the discrete fracture network. The generated discrete fracture network can reflect the heterogeneity of the actual fracture network in the whole simulation domain. Meanwhile, different well layouts will also impact the thermal recovery performance of the reservoir. In this work, we study the difference of heat extraction in heterogeneous fractured reservoirs under different injection modes to find the optimal thermal extraction.

Fig. 8 is the schematic diagram of four production and injection modes, where the orange area is the fractured reservoir, the red line represents the injection well, the blue line indicates the production well. Figs. 8(a) and (b) are parallel well configurations with injection on the dense fracture side and the sparse fracture side, respectively. Figs. 8(b) and (c) are anti-parallel well configurations with injection on the dense fracture side and the sparse fracture side, respectively.

The basic reservoir model setup and boundary conditions are shown in Fig. 9. The numerical simulation area is a 600×600m fractured reservoir composed of a rock matrix and a fracture network. As consistent with the fracturing process, the injection and production wells were specified as pipelines with different inlet and outlet on two sides of the reservoir. The remaining boundaries were set as impermeable and adiabatic conditions.

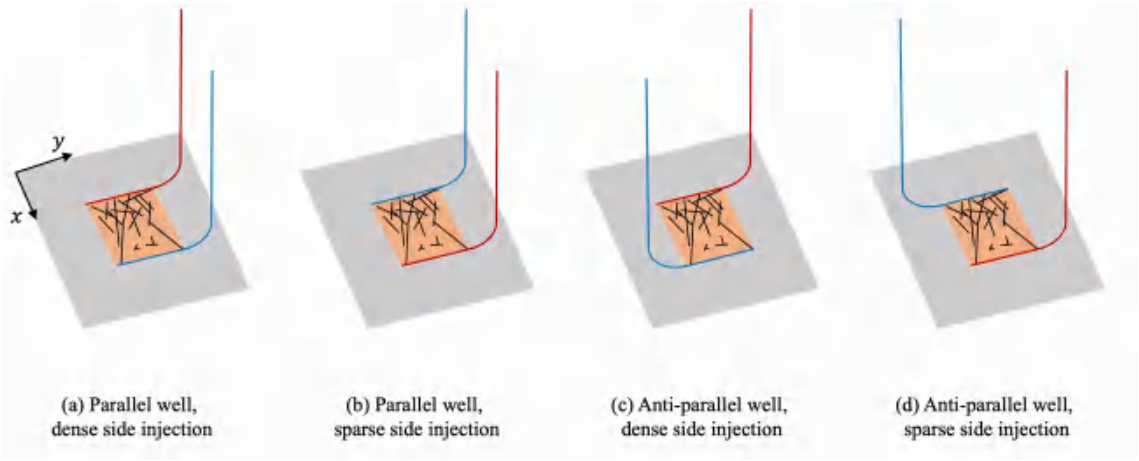

Figure 8: Schematic diagram of numerical model for different production and injection modes.

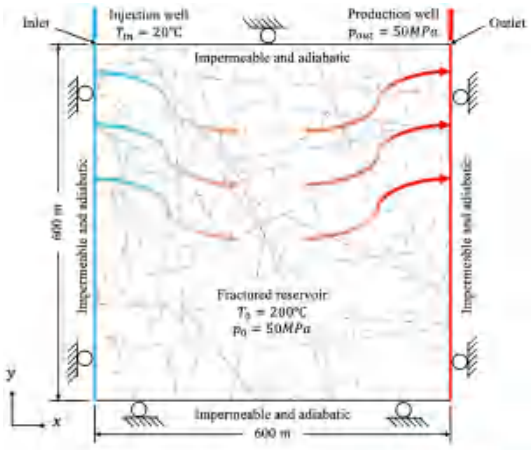

Figure 9: Illustration of basic reservoir model setup and boundary conditions.

The initial temperature of the reservoir is 200°C, and the temperature of the injection water is 20°C. The initial pressure of the reservoir is set as 50MPa. Impermeable and adiabatic conditions are applied to the perimeter boundaries of the reservoir. As for the mechanical field, all the outside surfaces are constrained at the normal direction. The relevant parameters for the numerical simulations are listed in Table 3 [29,35,36,38,45,46].

3.3 Definition of assessment parameters

In order to evaluate the production performance of the EGS, the corresponding evaluation parameters need to be defined. In this study, outlet average temperature, outlet

Table 3: Parameters for the simulations [29, 35, 36, 38, 47, 48].

Parameters	Unit	Value
Rock density ρ_m	kg/m^3	2700
Rock heat capacity c_m	$J/(kg\cdot K)$	1000
Elastic modulus	Pa	2.5×10^{-10}
Poisson ratio v		0.25
Biot-Wills coefficient α_B		1
Thermal expansion coefficient α_T	$1/K$	5×10^{-6}
Rock porosity		1%
Rock heat conductivity λ_m	$W/(m\cdot K)$	3.0
Rock permeability κ_m	m^2	1×10^{-18}
Rock specific storage S_m	1/Pa	1×10^{-8}
Water density ρ_f	kg/m^3	1000
Water heat capacity c_f	$J/(kg\cdot K)$	4200
Fracture aperture d_f	m	0.001
Fracture specific storage S_f	1/Pa	1.0×10^{-9}
Fracture porosity		99%
Fracture initial permeability κ_{f0}	m^2	1×10^{-11}

average thermal power and heat extraction ratio are adopted to assess the heat extraction performance in the geothermal reservoir.

The outlet average temperature is the key parameter for calculating the outlet average heat power, which can be defined as follow [48]:

$$T_{\text{out}} = \frac{\int_L T(t)dl}{L}, \tag{3.1}$$

where L is the total length of production well outlet and $T(t)$ denotes the outlet temperature of the production well at time t.

The outlet average thermal power P can be calculated by the following equation [47, 51]:

$$P = c_f Q(T_{\text{out}} - T_{\text{in}}), \tag{3.2}$$

where c_f is the heat capacity of water; Q is the outlet flow rate and T_{in} is temperature of the injected fluid.

The heat extraction ratio η is defined as the ratio of the cumulative thermal energy extracted to the extractable thermal energy of the geothermal reservoir, which can be described by the following equation [47]

$$\eta = \frac{\iint_S [T_0 - T_r(t)]dS}{\iint_S (T_0 - T_{in})dS}, \tag{3.3}$$

where T_0 is initial temperature of the reservoir and $T_r(t)$ denotes temperature of the reservoir at time t.

The accumulative extracted thermal energy ξ represents the total energy extracted during the production period. It can be calculated by the following equation [47]:

$$\xi = \int_0^t c_f Q(T_{\text{out}} - T_{\text{in}})dt. \tag{3.4}$$

4 Results and discussion

4.1 Effect of different production and injection modes on thermal performance

This part discusses the thermal recovery differences of the heterogeneous fractured reservoir under the same injection pressure (60MPa) with four different production and injection modes: parallel wells with fracture dense side injection, parallel wells with fracture sparse side injection, anti-parallel wells with fracture dense side injection, and anti-parallel wells with fracture sparse side injection. Here the fracture density of reservoir is set to be 0.05m^{-1}.

Fig. 10 show the temperature distribution at 3 years (first row) and 10 years (second row) with parallel well dense side injection (Fig. 10(a)), parallel well sparse side injection (Fig. 10(b)), anti-parallel well dense side injection (Fig. 10(c)) and anti-parallel well sparse side injection (Fig. 10(d)). In Figs. 10(a) and (c), for dense side injection, the anti-parallel well configuration has a longer fluid flow path through the reservoir compared to the parallel well configuration, a larger reservoir cooling zone, and a later time to thermal breakthrough than the parallel well configuration. With the parallel well configuration, the fluid inlet and outlet are located on the same side of the reservoir, and the pressure difference on the inlet-outlet sides is greater than anti-parallel well configuration, so that the fluid flows faster near the inlet-outlet side and the thermal breakthrough occurred earlier. This uneven distribution of flow results in that the heat extraction occurs mainly around the inlet-outlet side, and little thermal extraction occurs at other locations. On the contrary, thermal heat extraction is more uniform for the anti-parallel well configuration. In Figs. 10(b) and (d), the above phenomenon is also more obvious when injecting from the sparse side, so we can draw a conclusion that the anti-parallel well configuration is more favorable for reservoir heat extraction.

Figs. 10(c) and (d) show the temperature distributions for the anti-parallel well configuration. When injecting from the dense side of the fracture network (Fig. 10(c)), there are more fluid flow paths at the inlet, the resistance of fluid flow is smaller, the flow rate is faster, and the fluid distribution is more dispersed, so in the early stage of thermal extraction in the fracture density area of thermal extraction is faster, but in the later stage due to thermal breakthrough of the outlet temperature drop is also faster. When injecting from the sparse side of fracture network (Fig. 10(d)), because there are fewer fluid flow paths at the inlet, the resistance of fluid flow is higher, the temperature propagates along only a few fractures at the beginning, and the spread of low temperature zone is slower, and the heat extraction effect is poor. After that, as the low temperature zone

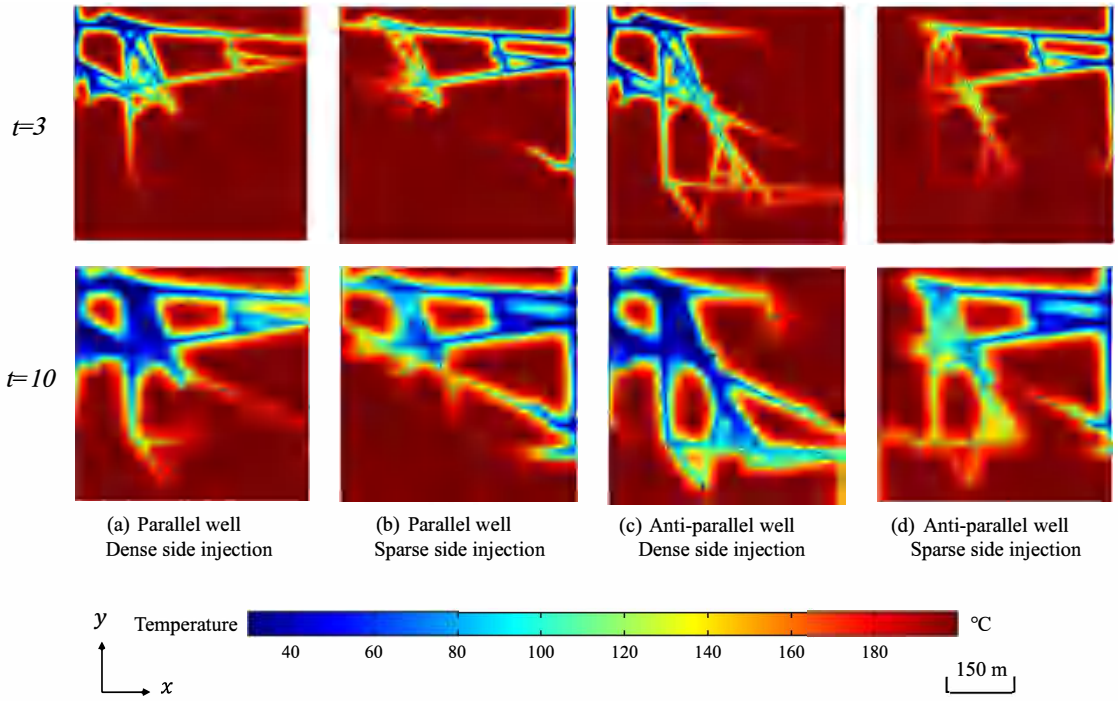

Figure 10: Temperature distribution in a typical heterogeneous fractured reservoir at 3 years (first row) and 10 years (second row) with different production and injection modes.

expands to the fracture intensive area, the fluid distribution in the fracture intensive area is more uniform, so the heat extraction conditions are better in the later stage, and the outlet temperature drops slowly after the thermal breakthrough.

Fig. 11(a) shows the variation of outlet temperature over the production time with the four injection-production modes. Parallel well configurations injecting on the dense or sparse side of the fracture have little difference in average outlet temperatures in the first two years, and the outlet temperature is slightly higher than that at the dense side in the later stage. For the anti-parallel well dense side injection, the outlet average temperature remains high for the first two years, and slowly decreases to 85°C after 20 years. With anti-parallel well sparse side injection, the average outlet temperature remains high for a longer period and then decreases more slowly to 130°C after 20 years. In general, the average outlet temperature of the anti-parallel well configuration is higher than that of the parallel well configuration, and the average outlet temperature is higher than that of the dense side when injecting from the sparse side of the fracture under the same well configuration.

Fig. 11(b) shows the evolution of outlet mass flow rate of parallel and anti-parallel well configurations with different injection modes. The mass flow rate of all injection-production modes increases rapidly in the early stage of production and then slowly

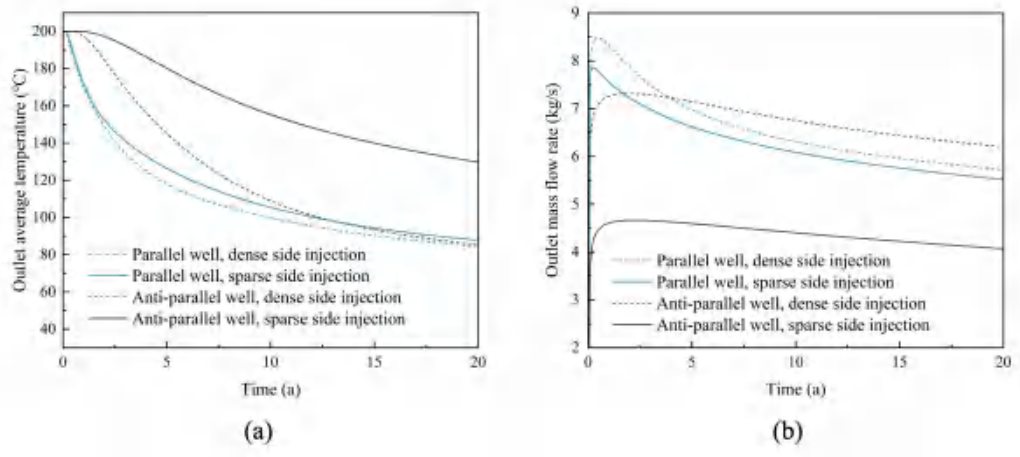

Figure 11: Variation of outlet average temperature (a) and outlet mass flow rate (b) over the production time.

decline. The outlet mass flow rate of the anti-parallel well sparse side injection configuration is significantly lower than other configurations. Under the same well configuration, the mass flow rate of dense side injection is significantly higher than that of the sparse side injection, which is mainly due to the fact that the dense fracture network can provide more flow paths for the fluids and conducive to fluid flow. As a result, the flow distribution in the area with dense fractures in the reservoir is more uniform. The overall mass flow rate is high in parallel well configuration, mainly because the distance between the inlet and outlet is close, and the shorter the distance under constant inlet and outlet pressure, the greater the pressure gradient, which is conducive to fluid flow.

Fig. 12 shows the variation of the outlet average thermal power and the heat extraction ratio over the production time. In Fig. 12(a), compared with the anti-parallel well configuration, the average thermal power at the outlet of the parallel well configuration remained at a high value in the first two years, and then decreased rapidly to be lower than that of the anti-parallel well configuration after four years. Under the same well configuration, the average thermal power at the outlet of dense side injection is higher than that of sparse side injection in the early stage, and lower than that of sparse side injection in the late stage. The main reason for this phenomenon is that the heat extraction at the dense fracture is better. Although the average outlet thermal power of the sparse side injection in the anti-parallel well configuration was the initially the lowest, its average outlet thermal power was the most stable and exceeded that of the other well configurations after 10 years. In Fig. 12(b), it can be seen that the heat extraction rate of dense side injection is generally higher than that of sparse side injection. Due to the premature thermal breakthrough, the heat extraction rate of the anti-parallel well configuration is higher than that of the parallel well configuration under the same injection conditions. The heat extraction rate of the reservoir is highest for the anti-parallel well configuration

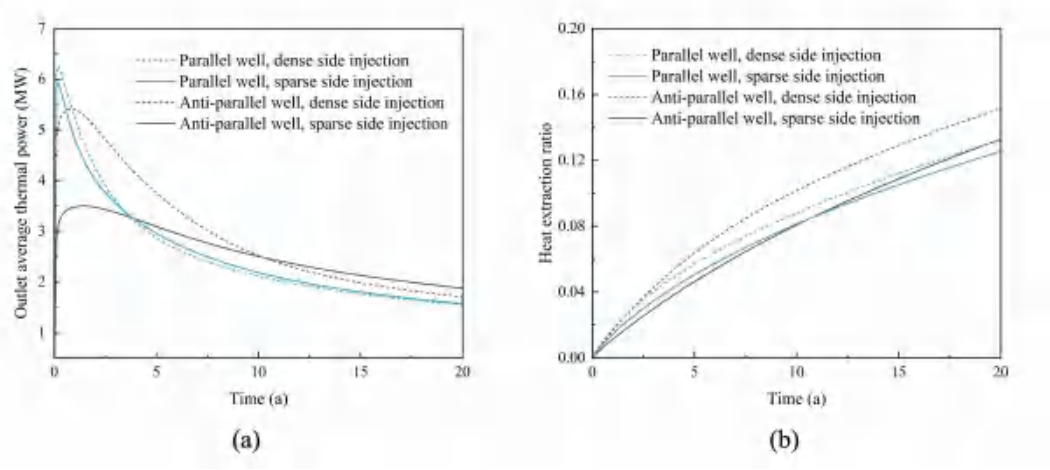

Figure 12: Variation of outlet average thermal power (a) and heat extraction ratio (b) over the production time.

with dense side injection and lowest for the parallel well configuration with sparse side injection. For anti-parallel well sparse side configurations, although the outlet average temperature remains stable, the heat extraction ratio is lower than dense side injection because its mass flow is lower.

In general, under the condition of same injection pressure, the thermal extraction performance of anti-parallel well configuration is better than parallel well configuration, and injection from the dense side of the fracture network is better than the sparse side for heterogeneous fractured reservoir. In Fig. 13, the accumulative extracted thermal energy and the heat extraction ratio of the reservoir after 20 years are the largest in the anti-parallel well configuration dense side injection. Under the same injection pressure, the heat extraction ratio and accumulative extraction thermal energy of the reservoir are the largest under the condition of dense side injection in the anti-parallel well configuration, so the heat extraction performance of the reservoir is the best when the dense side injection in the anti-parallel well configuration.

At the same time, we also analyzed the thermal extraction performance of the reservoir at a constant injection flow rate of 6kg/s, and the model parameters were set as above.

In Fig. 14(a), the average outlet temperature of the anti-parallel well configuration is generally higher than that of the parallel well configuration under constant injection flow and the time of thermal breakthrough occurs later, with the average outlet temperature being highest when the antiparallel well is injected on the sparse side. From the inlet pressure (Fig. 14(b)), it can be seen that the inlet pressure when injecting from the sparse side is generally higher than that from the dense side, and the inlet pressure when injecting from the sparse side of the anti-parallel well is the largest, so more energy is required for the same injection flow. In Figs. 14(c) and (d), the average outlet thermal power of the anti-parallel well configuration is higher than that of the parallel well configuration at

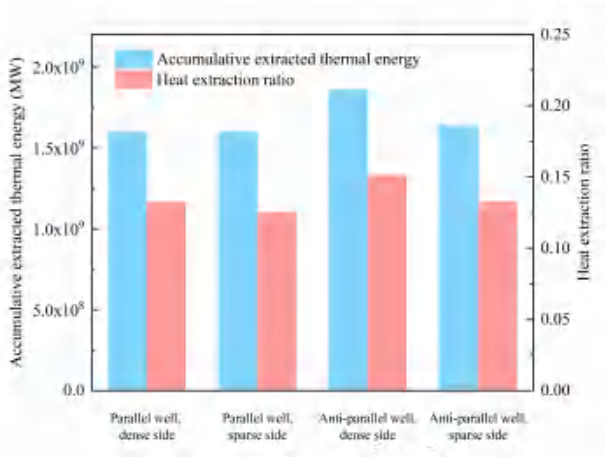

Figure 13: Accumulative extracted thermal energy and heat extraction ratio after 20 years of different production and injection modes.

the late stage of thermal extraction, and the anti-parallel well configuration has the most accumulative extracted thermal energy when injecting on the sparse side.

In general, the average outlet temperature is the highest, the accumulated extracted heat energy is the highest and the heat extraction effect is the best in the anti-parallel well configuration with sparse side injection, but the required inlet pressure is also the largest. However, the inlet pressure required for dense side injection in the anti-parallel well configuration is much lower, and a better heat extraction effect can be achieved. Therefore, we can draw the same conclusion under constant injection flow, that is, dense side injection in anti-parallel well configuration is the most conducive to reservoir heat extraction.

4.2 Influence of different fracture densities on thermal extraction performance of heterogeneous fractured reservoirs considering different injections

This section discusses the thermal recovery performance of heterogeneous fractured reservoirs with fracture densities of 0.025, 0.05 and 0.075m^{-1} under the anti-parallel well configuration. To avoid the effect of different mass flow rates on thermal recovery, here the mass flow rate of the injection well is set to be a constant value of 6kg/s.

Fig. 15 shows the temperature distribution of heterogeneous fractured reservoirs with different fracture densities over 10 years. It can be seen that the thermal extraction performance of the reservoir is significantly different under different fracture densities. When the fracture density is low (0.025m^{-1}, Fig. 15(a)), the thermal extraction of the reservoir occurs around a few connected fractures. As the fracture density increases (Figs. 15(b) and (c)), the thermal extraction of the reservoir becomes more and more uniform.

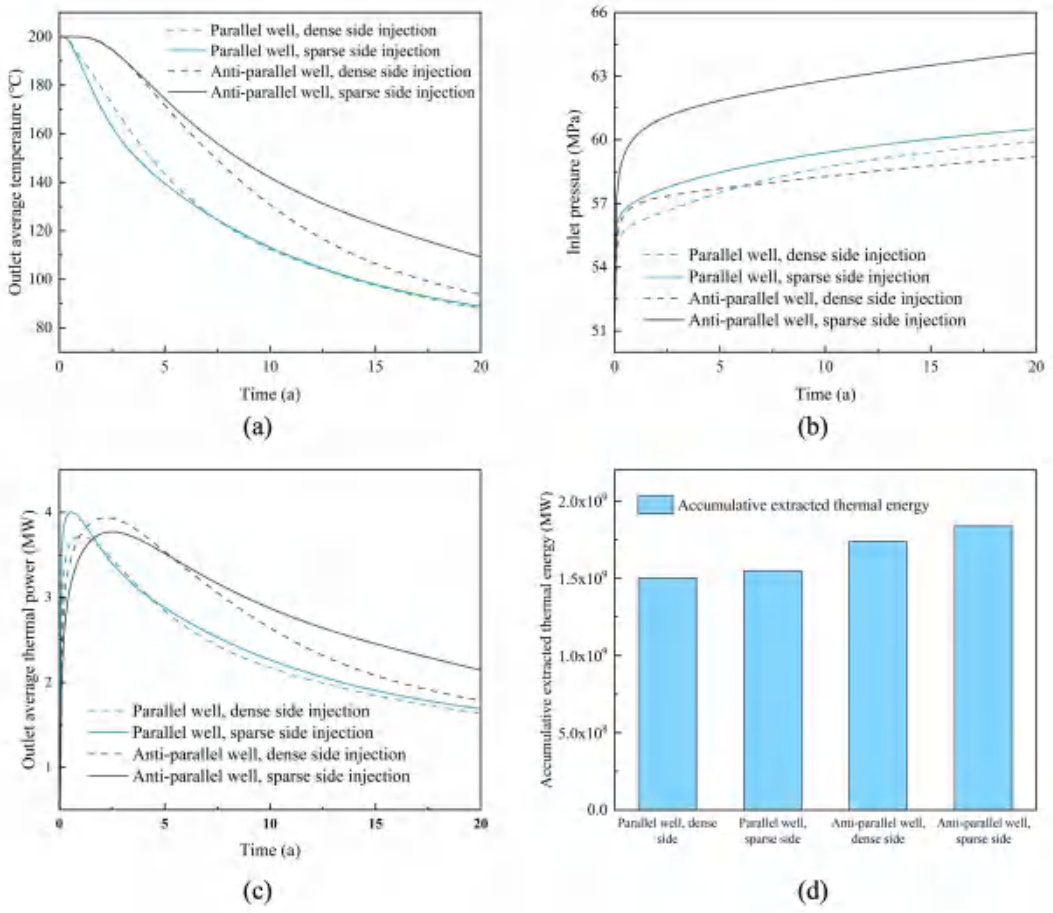

Figure 14: Outlet average temperature (a), inlet pressure (b), outlet average thermal power (c) and accumulative extracted thermal energy (d) of reservoir at constant injection flow rate (6kg/s).

Figs. 16(a) and (b) shows the variation of outlet average temperature and inlet pressure during EGS operation. Both dense side and sparse side injection are investigated under different fracture densities. One can see that the average outlet temperature is directly proportional to the fracture density, and the inlet pressure is inversely proportional to the fracture density. At the same injection flow rate, the average outlet temperature of sparse side injection is higher than that of dense side injection. Although the sparse-side injection is not conducive to fluid flow, the thermal extraction performance will be better with the same injection mass flow rate.

Figs. 16(c) and (d) shows the outlet average thermal power and the thermal extraction ratio for the dense-side and sparse side injections under different fracture densities. One can also see that, the outlet average thermal power and the thermal extraction ratio will be larger with higher fracture density. Moreover, the outlet average thermal power and

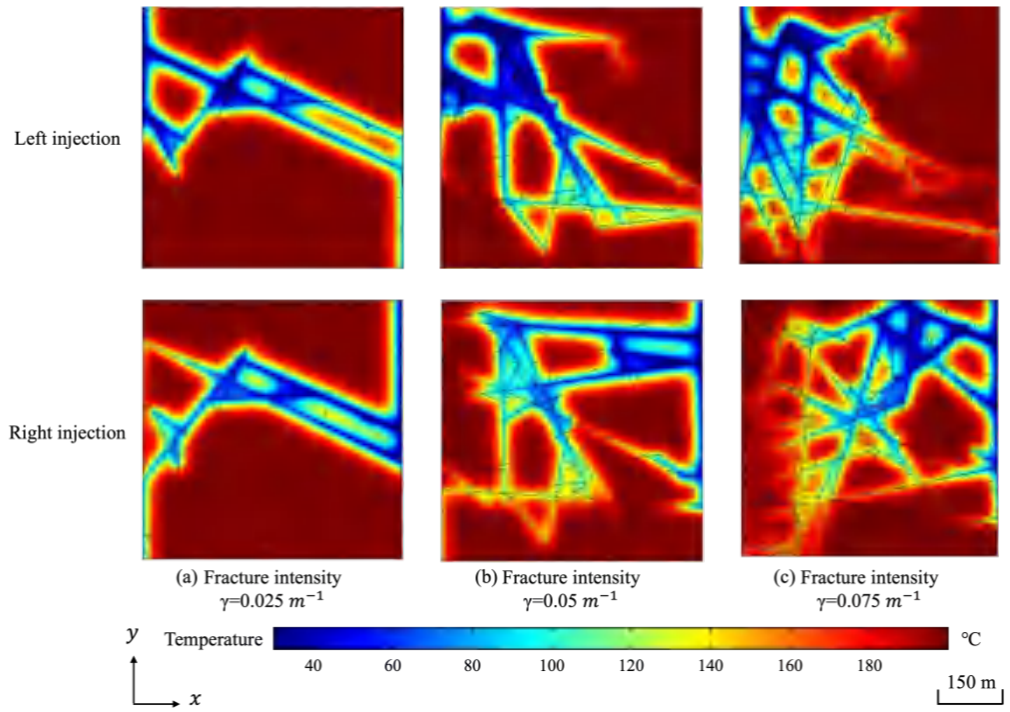

Figure 15: Temperature distribution in heterogeneous fracture networks at 10 years with various fracture intensities γ, considering both dense-side and sparse-side injection.

the thermal extraction ratio will be larger with the sparse-side injection than dense-side injection under the condition of same mass flow rate.

In general, the higher the fracture density, the better the thermal extraction effect of the reservoir. Under the same fracture density, the thermal extraction effect of the sparse side injection in the anti-parallel well configuration is better than that of the dense side injection. At the same injection flow rate, the disadvantage of injection from the sparse fracture side is that it requires a large injection pressure. In Fig. 17, when the fracture density is 0.075m^{-1} fracture sparse side injection, the cumulative extracted heat energy and heat extraction rate of the reservoir are the largest, which are 2.3×10^{9}MW and 0.172, respectively. When the fracture density is 0.025m^{-1} fracture sparse side injection, the cumulative extracted thermal energy and thermal extraction rate of the reservoir are the lowest, which are 1.1×10^{9}MW and 0.088, respectively.

4.3 Stress field evolution and sensitivity analysis

This section employs the numerical model of an anti-parallel well configuration with fracture dense side injection, as presented in Section 4.1, to illustrate the stress evolution of a fractured reservoir during the heat recovery process. Furthermore, the effect of key

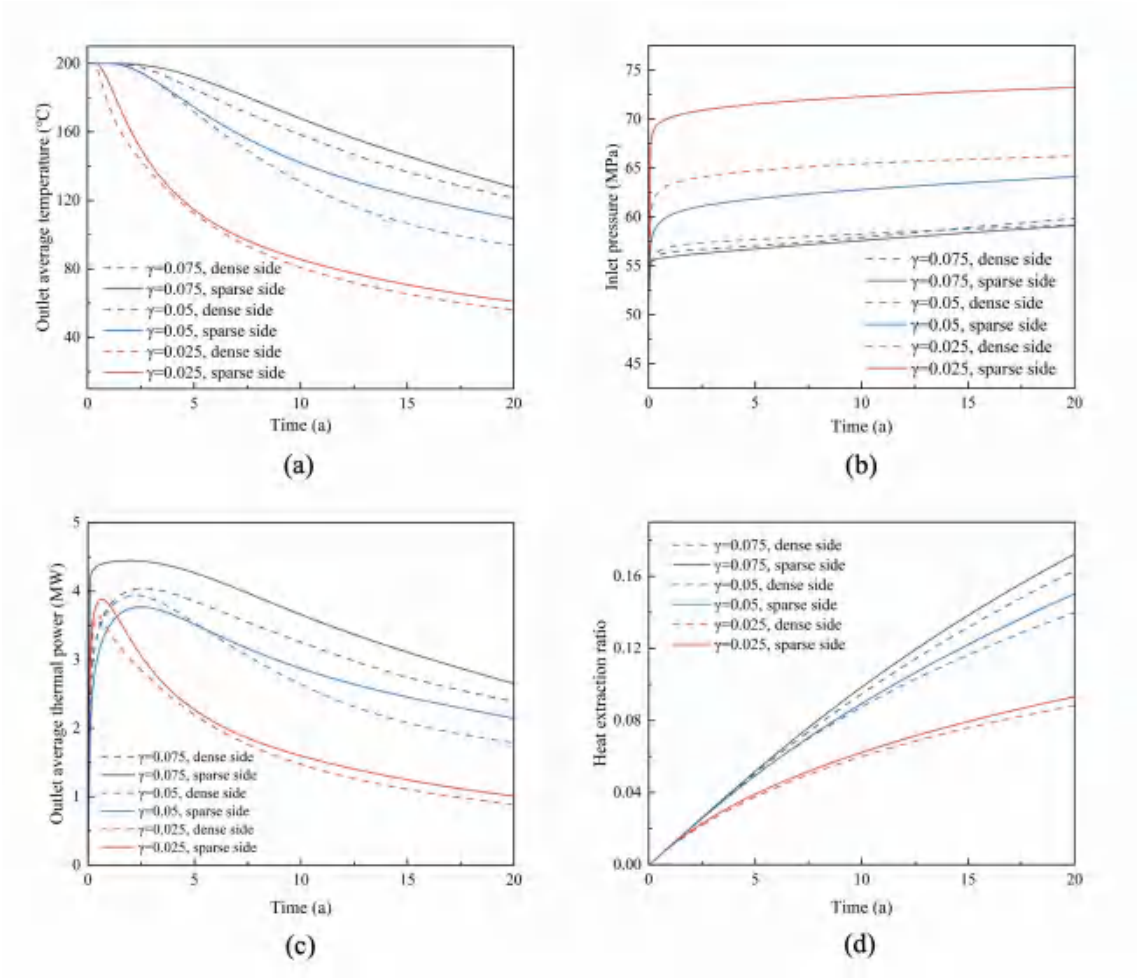

Figure 16: Variation of outlet average temperature (a), inlet pressure (b), outlet average thermal power (c) and heat extraction ratio (d) over the production time.

parameters (including injection pressure and mass flow rate) on the heat recovery process is conducted.

4.3.1 Stress evolution during thermal recovery

The parameter settings of the numerical model in this section are identical to those in Section 4.2, and the mass flow rate at the inlet is 6kg/s. Low temperature fluid is injected into the reservoir from the upper-left corner inlet and extracted from the lower-right corner outlet. The evolution of stress field is primarily influenced by two factors: pressure diffusion caused by fluid flow, and thermal stress caused by temperature difference in heat transfer. Pressure diffusion is primarily demonstrated in the preceding years, while the thermal stress will affect the stress distribution of rock matrix in the long run of thermal

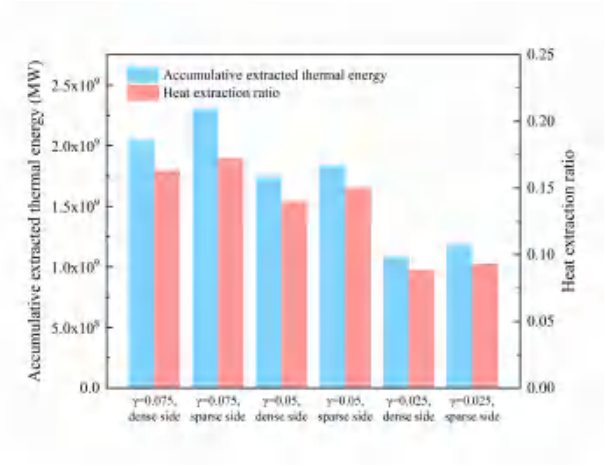

Figure 17: Accumulative extracted thermal energy and heat extraction ratio after 20 years.

exploitation.

Fig. 18 illustrates the evolution of stress field in a typical fractured reservoir at different time. In the initial phase of thermal exploitation (Fig. 18(a)), high stress is primarily observed near the fractures at the entrance. The high permeability of fracture allows fluid pressure to propagate along the fracture network from the inlet to the outlet. But the low-temperature region is primarily situated in close proximity to the inlet. Consequently, the thermal stresses are mainly concentrated in the vicinity of the inlet.

As thermal exploitation progresses, the low-temperature region gradually extends along the fracture network towards the outlet. Therefore, as illustrated in Fig. 18(b), the stress field gradually propagates along the fracture network. In the subsequent long-term thermal exploitation, the temperature field evolves gradually towards a state of stability, with the low-temperature region spreading from the vicinity of the fracture to the interior of the rock matrix. Similarly, the thermal stress caused by temperature difference evolutes towards the interior of matrix, as shown in Fig. 18(c). Finally, after 20 years (Fig. 18(d)), followed by a gradual stabilization of temperature field, the stress field reaches a state of equilibrium.

4.3.2 Effect of key parameters on heat recovery

In this section, we investigated the effects of two key parameters, injection pressure and mass flow rate, on the thermal extraction performance.

Fig. 19 shows the thermal extraction performance of the reservoir under different injection pressures. As the injection pressure increases, the outlet mass flow rate of the fluid also increases (Fig. 19(a)). The increase in flow rate results in an increase of heat transfer efficiency, meanwhile leading to a decline in outlet temperature (Fig. 19(b)). The outlet average thermal power increases with the increase of injection pressure. However, as the heat recovery continues, the increase in pressure difference has a smaller effect

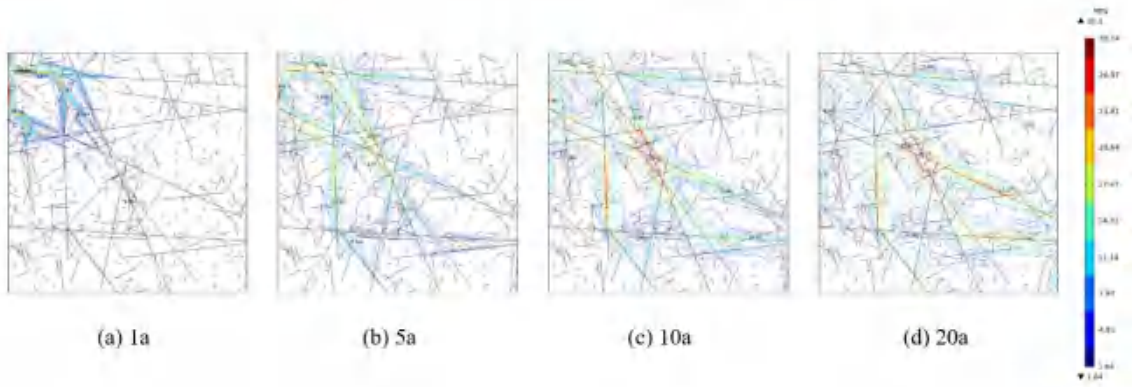

Figure 18: Evolution of stress field in a typical heterogeneous fractured reservoir at different time.

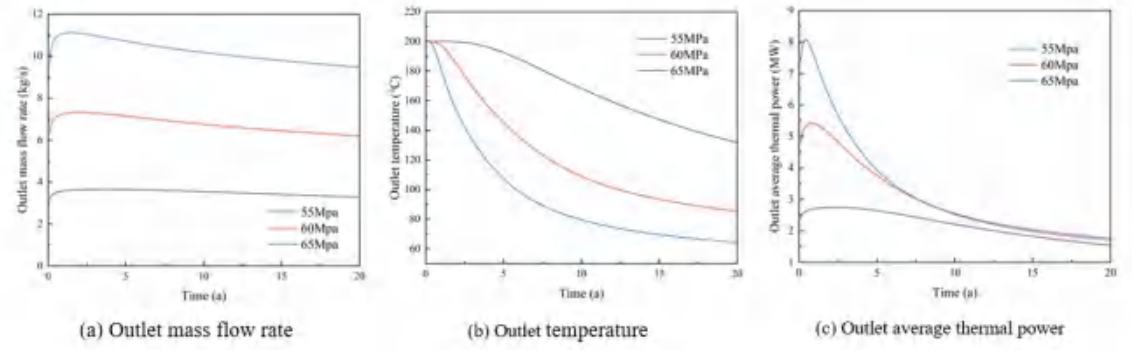

Figure 19: Thermal extraction performance under different injection pressures (outlet pressure 50Mpa).

on the outlet average thermal power, as shown in Fig. 19(c). Consequently, excessive injection pressure will result in a shortened lifespan of EGS and a rapid decline in the average outlet thermal power. This is in agreement with the simulation results presented of Zhang [38].

Fig. 20 shows the thermal extraction performance of the reservoir under different mass flow rates. As the injection mass flow rate increases, the injection pressure of the fluid also increases (Fig. 20(a)). The increase in flow rate leads to insufficient heat transfer of the fluid, resulting in a decrease in outlet temperature (Fig. 20(b)). The outlet average thermal power increases with the increase of injection mass flow rate, but as heat recovery progresses, the increase in injection flow rate leads to a smaller increase in the outlet average thermal power, while the injection pressure requirement becomes higher, as illustrated in Figs. 20(a) and (c). Consequently, an excessive inlet mass flow rate can also result in a shortened lifespan of EGS and a rapid decline in the outlet average thermal power.

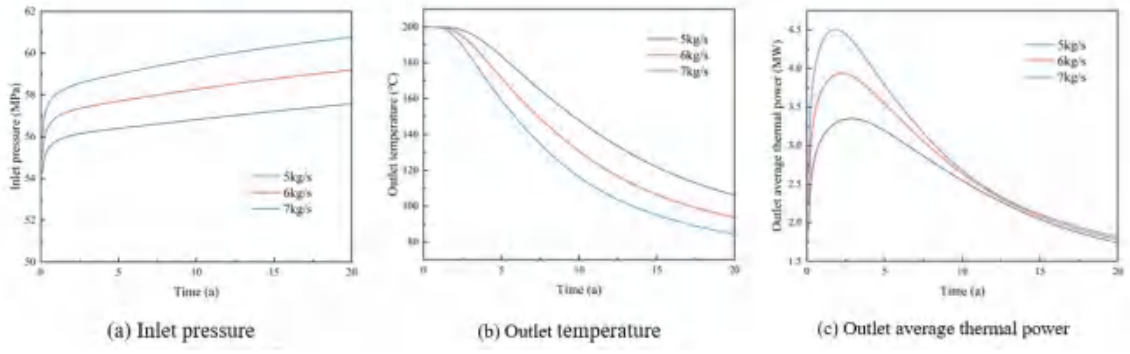

Figure 20: Thermal extraction performance under different mass flow rate.

5 Conclusions

In this work, the thermal extraction performance of geothermal reservoirs with heterogeneous fracture network is investigated under different injection-production schemes. First, a heterogeneous discrete fracture network generation method is proposed based on the relative distribution of pressure in reservoir. A thermal-hydraulic-mechanical (THM) coupling model is established to simulate the fluid-flow and heat-transfer processes in fractured reservoirs. The accuracy of the proposed model is verified by comparing the simulation results of a single fracture model and a linear elastic column model with the analytical results. Then, the model is applied to EGS to study the thermal extraction performance of different injection-production methods of heterogeneous fractured reservoirs to find a better heat extraction method. By coupling the THM process, methods to improve the thermal extraction efficiency of heterogeneous fractured reservoirs were studied. The evolution of stress field during the heat extraction process, and the effects of key parameters are also presented.

The following conclusion can be obtained:

(1). Under the same injection pressure, anti-parallel wells are less susceptible to thermal breakthrough than parallel wells. The mass flow rate of injection on the sparse side is lower than that on the dense side. The maximum accumulative extracted thermal energy and heat extraction ratio of 1.86×10^9MW and 0.151 for anti-parallel wells with dense side injection are 16.56% and 14.30% higher than those for parallel wells with dense side injection, respectively.

(2). Under the constant injection flow rate, the reservoir outlet average temperature is higher with the anti-parallel well configuration, and requires a higher inlet pressure when injecting from the fracture sparse side. The maximum cumulative heat extracted with the sparse side injection for the anti-parallel well is 1.84×10^9MW, which is 22.33% higher than the dense side injection with parallel wells. Consider-

ing the injection pressure, the dense-side injection for the anti-parallel well configuration is more efficient for heat extraction.

(3). For the anti-parallel well configuration with the same mass flow rate, the heat recovery performance of reservoir (i.e., outlet temperature, outlet thermal power and heat extraction ratio) is positively correlated with fracture density of reservoir. Sparse-side injection yields better heat recovery performance than dense-side injection for different fracture densities.

(4). For the anti-parallel well configuration with the same mass flow rate, when the fracture density is 0.075m^{-1}, the sparse side injection yields an accumulative extracted thermal power of 2.3×10^{9}MW and a heat extraction ratio of 0.172. These values are 12.86% and 5.56% higher than those of dense side injection, respectively, and 95.65% and 84.97% higher than those with a fracture density of 0.025m^{-1}, respectively. Thus, the thermal extraction performance of the reservoir can be effectively improved by using sparse-side injection or increasing fracture density at the same injection flow rate.

(5). The stress field of the reservoir during thermal exploitation exhibit the characteristics of rapid propagation in the early stage and slow stabilization changes in the later stage. Sensitivity analysis of mass flow rate and injection pressure indicates that excessive mass flow rate and injection pressure are not conducive to thermal extraction of the reservoir.

The research results can provide reference for the design and planning of Geothermal Engineering. In the future, three-dimensional model can be developed to fully capture the intricacies of geothermal reservoirs.

Acknowledgements

The research was supported by the Key Research and Development Program of China (No. 2021YFB150740502).

References

[1] P. Olasolo, M. C. Juarez, J. Olasolo, M. P. Morales and D. Valdani, *Economic analysis of Enhanced Geothermal Systems (EGS). A review of software packages for estimating and simulating costs,* Appl. Thermal Eng., 104 (2016), pp. 647–658.
[2] A. Pollack and T. Mukerji, *Accounting for subsurface uncertainty in enhanced geothermal systems to make more robust techno-economic decisions,* Appl. Energy, 254 (2019), 113666.
[3] J. W. Lund and A. N. Toth, *Direct utilization of geothermal energy 2020 worldwide review,* Geothermics, 90 (2021), 101915.
[4] S. M. Lu, *A global review of enhanced geothermal system (EGS),* Renewable Sustainable Energy Rev., 81 (2018), pp. 2902–2921.

[5] J. L. ZHU, K. Y. HU, X. L. LU, X. X. HUANG, K. T. LIU AND X. J. WU, *A review of geothermal energy resources, development, and applications in China: Current status and prospects,* Energy, 93 (2015), pp. 466–483.

[6] R. SHORTALL, B. DAVIDSDOTTIR AND G. AXELSSON, *Geothermal energy for sustainable development: A review of sustainability impacts and assessment frameworks,* Renewable Sustainable Energy Rev., 44 (2015), pp. 391–406.

[7] R. BARIA, J. BAUMGARTNER, F. RUMMEL, R. J. PINE AND Y. SATO, *HDR/HWR reservoirs: concepts, understanding and creation,* Geothermics, 28(4-5) (1999), pp. 533–552.

[8] A. KAMALI, A. GHASSEMI AND D. KUMAR, *3D modeling of hydraulic and natural fracture interaction,* Rock Mech. Rock Eng., 56(2) (2022), pp. 875–893.

[9] W. G. P. KUMARI, P. G. RANJITH, M. S. A. PERERA, X. LI, L. H. LI, B. K. CHEN, B. L. AVANTHI ISAKA AND V. R. S. DE SILVA, *Hydraulic fracturing under high temperature and pressure conditions with micro CT applications: Geothermal energy from hot dry rocks,* Fuel, 230 (2018), pp. 138–154.

[10] H. Z. WANG, G. S. LI, Z. H. SHEN, S. C. TIAN, B. J. SUN, Z. G. HE AND P. Q. LU, *Experiment on rock breaking with supercritical carbon dioxide jet,* Journal of Petroleum Science and Engineering, 127 (2015), pp. 305–310.

[11] X. W. ZHANG, Y. Y. LU, J. R. TANG, Z. ZHOU AND Y. LIAO, *Experimental study on fracture initiation and propagation in shale using supercritical carbon dioxide fracturing,* Fuel, 190 (2017), pp. 370–378.

[12] X. LIANG, P. HOU, Y. XUE, X. Z. YANG, F. GAO AND J. LIU, *A fractal perspective on fracture initiation and propagation of reservoir rocks under water and nitrogen fracturing,* Fractals-Complex Geometry Patterns and Scaling in Nature and Society, 29(07) (2021), 2150189.

[13] S. TARASOV AND A. GHASSEMI, Radial Cracking of a Borehole by Pressure and Thermal Shock, 46th U.S. Rock Mechanics/Geomechanics Symposium, 2012, 24-27.

[14] Q. H. WU, L. WENG, Y. L. ZHAO, B. H. GOU AND T. LUO, *On the tensile mechanical characteristics of fine-grained granite after heating/cooling treatments with different cooling rates,* Eng. Geology, 253 (2019), pp. 94–110.

[15] W. G. P. KUMARI, P. G. RANJITH, M. S. A. PERERA, B. K. CHEN AND I. M. ABDULAGATOV, *Temperature-dependent mechanical behaviour of Australian Strathbogie granite with different cooling treatments,* Eng. Geology, 229 (2017), pp. 31–44.

[16] X. J. LI, G. S. LI, W. YU, H. Z WANG, K. SEPEHRNOORI, Z. M. CHEN, H. SUN AND S. K. ZHANG, *Thermal effects of liquid/supercritical carbon dioxide arising from fluid expansion in fracturing,* SPE J., 23(6) (2018), pp. 2026–2040.

[17] F. KUCHUK, D. BIRYUKOV AND T. FITZPATRICK, *Fractured-reservoir modeling and interpretation,* SPE J., 20(5) (2015), pp. 983–1004.

[18] L. C. BURROWS, F. HAERI, P. CVETIC, S. SANGUINITO, F. SHI, D. TAPRIYAL, A. GOODMAN AND R. M. ENICK, *A literature review of CO2, natural gas, and water-based fluids for enhanced oil recovery in unconventional reservoirs,* Energy Fuels, 34(5) (2020), pp. 5331–5380.

[19] A. D. TALEGHANI, M. GONZALEZ-CHAVEZ, H. YU AND H. ASALA, *Numerical simulation of hydraulic fracture propagation in naturally fractured formations using the cohesive zone model,* Journal of Petroleum Science and Engineering, 165 (2018), pp. 42–57.

[20] F. M. JIANG, J. L. CHEN, W. B. HUANG AND L. LUO, *A three-dimensional transient model for EGS subsurface thermo-hydraulic process,* Energy, 72 (2014), pp. 300–310.

[21] S. Q. HE, B. FENG, J. S. ZHU, X. Y. LIU, S. T. SHANGGUAN, X. F. QI AND J. L. LIU, *A 3D analysis of the occurrence of fractures in hot dry rock reservoirs based on the spatial distribution of natural fractures,* Energy Geosci., 4 (2023), 100165.

[22] Y. Y. MA, S. B. LI, L. G. ZHANG, S. Z. LIU, Z. Y. LIU, H. LI AND E. X. SHI, *Study on the effect of well layout schemes and fracture parameters on the heat extraction performance of enhanced geothermal system in fractured reservoir,* Energy, 202 (2020), 117811.

[23] X. X. LI, C. Y. LI, W. P. GONG, Y. J. ZHANG AND J. C. WANG, *Probabilistic analysis of heat extraction performance in enhanced geothermal system based on a DFN-based modeling scheme,* Energy, 263(c) (2023), 125674.

[24] F. S. ZHANG, B. DAMJANAC AND S. MAXWELL, *Investigating hydraulic fracturing complexity in naturally fractured rock masses using fully coupled multiscale numerical modeling,* Rock Mech. Rock Eng., 52(12) (2019), pp. 5137–5160.

[25] X. ZHANG, Z. Q. HUANG, Q. H. LEI, J. YAO, L. GONG, W. D. YANG, X. YAN AND Y. LI, *Improving heat extraction performance of enhanced geothermal systems: Insights from critical fracture network parameter and multi-objective optimization method,* Appl. Thermal Eng., 213 (2022), 118671.

[26] Y. SHI, X. Z. SONG, J. C. LI, G. S. WANG, F. X. YULONG AND L. D. GENG, *Analysis for effects of complex fracture network geometries on heat extraction efficiency of a multilateral-well enhanced geothermal system,* Appl. Thermal Eng., 159 (2019), 113828.

[27] Y. Q. LIAO, X. H. SUN, B. J. SUN, J. C. XU, D. HUANG AND Z. Y. WANG, *Coupled thermal model for geothermal exploitation via recycling of supercritical CO2 in a fracture-wells system,* Appl. Thermal Eng., 159 (2019), 113890.

[28] Q. L. CHENG, X. N. WANG AND A. GHASSEMI, *Numerical simulation of reservoir stimulation with reference to the Newberry EGS,* Geothermics, 77 (2019), pp. 327–343.

[29] Y. SHI, X. Z. SONG, G. S. WANG, J. C. LI, L. D. GENG AND X. J. LI, *Numerical study on heat extraction performance of a multilateral-well enhanced geothermal system considering complex hydraulic and natural fractures,* Renewable Energy, 141 (2019), pp. 950–963.

[30] P. ASAI, R. PODGORNEY, J. MCLENNAN, M. DEO AND J. MOORE, *Analytical model for fluid flow distribution in an Enhanced Geothermal Systems (EGS),* Renewable Energy, 193 (2022), pp. 821–831.

[31] B. BERKOWITZ, *Characterizing flow and transport in fractured geological media: A review,* Adv. Water Res., 25(8-12) (2002), pp. 861–884.

[32] A. ROULEAU AND J. E. GALE, *Statistical characterization of the fracture system in the stripa granite, Sweden,* Int. J. Rock Mech. Mining Sci., 22(6) (1985), pp. 353–367.

[33] A. FOX, P. LA POINTE, A. SIMEONOV, J. HERMANSON AND J. OEHMAN, *Statistical geological discrete fracture network model,* Forsmark Modelling Stage 2.2. Sweden: N. p., 2007, Web.

[34] O. BOUR AND P. DAVY, *Connectivity of random fault networks following a power law fault length distribution,* Water Res. Research, 33(7) (1997), pp. 1567–1583.

[35] Z. X. SUN, X. ZHANG, Y. XU, J. YAO, H. X. WANG, S. H. LV, Z. L. SUN, Y. HUANG, M. Y. CAI AND X. X. HUANG, *Numerical simulation of the heat extraction in EGS with thermal-hydraulic-mechanical coupling method based on discrete fractures model,* Energy, 120 (2017), pp. 20–33.

[36] F. C. GONG, T. K. GUO, W. SUN, Z. M. LI, B. YANG, Y. M. CHEN AND Z. Q. QU, *Evaluation of geothermal energy extraction in Enhanced Geothermal System (EGS) with multiple fracturing horizontal wells (MFHW),* Renewable Energy, 151 (2020), pp. 1339–1351.

[37] J. YAO, X. ZHANG, Z. X. SUN, Z. Q. HUANG, J. R. LIU, Y. LI, Y. XIN, X. YAN AND W. Z. LIU, *Numerical simulation of the heat extraction in 3D-EGS with thermal hydraulic-mechanical coupling method based on discrete fractures model,* Geothermics, 74 (2018), pp. 19–34.

[38] W. ZHANG, Z. Q. QU, T. K. GUO AND Z. Y. WANG, *Study of the enhanced geothermal system (EGS) heat mining from variably fractured hot dry rock under thermal stress,* Renewable Energy,

143 (2019), pp. 855–871.

[39] X. X. LI, D. Q. LI AND Y. XU, *Equivalent simulation method of three-dimensional seepage and heat transfer coupling in fractured rock mass of geothermal-borehole system,* Eng. Mech., 36(7) (2019), pp. 238–247.

[40] J. ZHENG, P. LI, B. DOU, T. FAN, H. TIAN AND X. T. LAI, *Impact research of well layout schemes and fracture parameters onheat production performance of enhanced geothermal system considering water cooling effect,* Energy, 225 (2022), 124496.

[41] T. K. GUO, S. J. TANG, J. SUN, F. C. GONG, X. Q. LIU, Z. Q. QU AND W. ZHANG, *A coupled thermalhydraulic-mechanical modeling and evaluation of geothermal extraction in the enhanced geothermal system based on analytic hierarchy process and fuzzy comprehensive evaluation,* Appl. Energy, 258 (2020).

[42] S. SAEID, R. AL-KHOURY AND F. BARENDS, *An efficient computational model for deep low-enthalpy geothermal systems,* Comput. Geosci., 51 (2013), pp. 400–409.

[43] X. HUANG, J. ZHU, J. LI, C. LAN AND X. J. JIN, *Parametric study of an enhanced geothermal system based on thermo-hydro-mechanical modeling of a prospective site in Songliao Basin,* Appl. Thermal Eng., 105 (2016), pp. 1–7.

[44] S. A. MILLER, *Modeling enhanced geothermal systems and the essential nature of large-scale changes in permeability at the onset of slip,* Crustal Permeability, 15 (1-2) (2015), pp. 338–349.

[45] H. A. LAUWERIER, *The transport of heat in an oil layer caused by the injection of hot fluid,* Appl. Sci. Res. Section A, 5(2) (1955), pp. 145–150.

[46] F. B. J. BARENDS, *Complete solution for transient heat transport in porous media, following Lauwerier's concept,* SPE Annual Technical Conference and Exhibition, SPE, 2010, SPE-134670-MS.

[47] X. Z. SONG, Y. SHI, G. S. LI, R. Y. YANG, G. S. WANG, R. ZHENG, J. C. LI AND Z. H. LYU, *Numerical simulation of heat extraction performance in enhanced geothermal system with multilateral wells,* Appl. Energy, 218 (2018), pp. 325–337.

[48] Y. Y. MA, S. B. LI, L. G. ZHANG, S. Z. LIU, Z. Y. LIU, H. LI, E. X. SHI AND H. J. ZHANG, *Numerical simulation study on the heat extraction performance of multi-well injection enhanced geothermal system,* Renewable Energy, 151 (2020), pp. 782–795.

[49] B. BAI, *One-dimensional thermal consolidation characteristics of geotechnical media under non-isothermal condition,* Eng. Mech., 22(5) (2005), pp. 186–191.

[50] Y. SHI, X. Z. SONG, J. C. LI, G. S. WANG, R. ZHENG AND F. X. YULONG, *Numerical investigation on heat extraction performance of a multilateral-well enhanced geothermal system with a discrete fracture network,* Fuel, 244 (2019), pp. 207–226.

[51] T. K. GUO, F. C. GONG, X. Z. WANG, Q. LIN, Z. Q. QU AND W. ZHANG, *Performance of enhanced geothermal system (EGS) in fractured geothermal reservoirs with CO2 as working fluid,* Appl. Thermal Eng., 152 (2019), pp. 215–230.